Materials Advances

ROYAL SOCIETY OF CHEMISTRY

PAPER

View Article Online
View Journal | View Issue

Cite this: *Mater. Adv.*, 2025, 6, 400

Denatured bovine serum albumin particle decorated graphene oxide nanocomposite for ultrasensitive resistive humidity sensing†

Pan Qi, Yongkang Zhang, Ziang Zhang, Xiaobing Li and Cunlan Guo *

Received 18th August 2024,
Accepted 27th November 2024

DOI: 10.1039/d4ma00832d

rsc.li/materials-advances

From humidity monitoring in various fields to noncontact human–machine interactions, the application of humidity sensors has been expanding. Accordingly, better resolution and higher sensitivity are desired for improving the performance of humidity sensors. In this study, an electrical sensor for highly sensitive humidity detection was fabricated *via* hydrogen bonding by integrating denatured bovine serum albumin particles (dBSA) with proton conductivity and graphene oxide (GO) nanosheets with large specific surface areas. The current signal of the sensor exhibits an approximately semi-logarithmic linear relationship with the relative humidity (RH), showing a nearly seven order of magnitude increase in current over the RH range of 15% to 90%. The sensor also displays high stability, selectivity, and response rate within a few seconds. The dBSA–GO nanofilm based humidity sensor was successfully applied to monitor respiration rates and simulate human–machine interaction in real time with high accuracy. Impedance spectroscopy and Kelvin probe measurements revealed the changes in the capacitance and work function of the dBSA–GO nanofilm with water adsorption. The water penetrating into the dBSA–GO nanofilm forms extensive hydrogen bonding networks, enhancing proton conductivity, while water adsorption on the surface alters dipole moments, resulting in asymmetric current behavior with increased current at forward bias. The extremely high humidity response shows the great potential of proteins in humidity sensor applications, thus expanding the field of biocompatible humidity sensors.

1. Introduction

With the rapid development of intelligent electronics, issues ranging from viral infection to human–machine interaction[1] through physical contact have received growing attention. The noncontact sensing capacity of humidity sensors[2,3] achieved by detecting the movement of moist human skin[4,5] provides a promising strategy to address this concern. In addition, humidity sensors are used for real-time humidity monitoring in many emerging fields, such as respiratory behavior,[6] speech recognition,[7] skin moisture,[8] and diaper monitoring.[9] These special application scenarios require the sensor to rapidly track the position and movement of local humidity sources and sensitively monitor their humidity levels.

Currently, most humidity-sensitive materials are based on the Grotthuss mechanism of proton hopping along the hydrogen bond chain with the participation of water.[10–14] The content of water is sensitively related to the proton transport and can be reflected by the electrical signal converted from proton transport.[15,16] This requires materials with abundant hydrophilic groups and large specific surface areas to provide enough sites and space for water molecule binding. Proteins are well-known proton transport materials.[17] Among them, bovine serum albumin (BSA) has great potential as a humidity sensing material due to its rich composition and water uptake capacity.[16,18–22] A drop-cast BSA film achieved a 350-fold decrease in resistance upon the relative humidity (RH) increasing from 60% to 80%.[16] However, the humidity sensing function of natural BSA films has not been satisfactory due to their limited long-term stability and moderate sensing performance. The denaturation and doping of BSA are promising approaches to tackle these challenges.[19,22] Therefore, we hypothesized that concurrent enhancements in stability and sensing capabilities could be achieved by synergistically integrating the benefits of both doping and denaturation.

BSA can be unfolded by reducing its disulfide bonds using tris(2-carboxyethyl)phosphine (TCEP), which leads to subsequent particle aggregation through hydrophobic interactions. These denatured BSA particles (dBSA) can assemble at air–liquid and solid–liquid interfaces through multiple interactions and form macroscopic two-dimensional nanofilms.[23,24] The nanofilms possess robust interfacial adhesion, abundant hydrogen bonds from β-sheet structures, and a variety of exposed

College of Chemistry and Molecular Sciences, Wuhan University, 299 Bayi Road, Wuhan, Hubei, 430072, China. E-mail: cunlanguo@whu.edu.cn

† Electronic supplementary information (ESI) available. See DOI: https://doi.org/10.1039/d4ma00832d

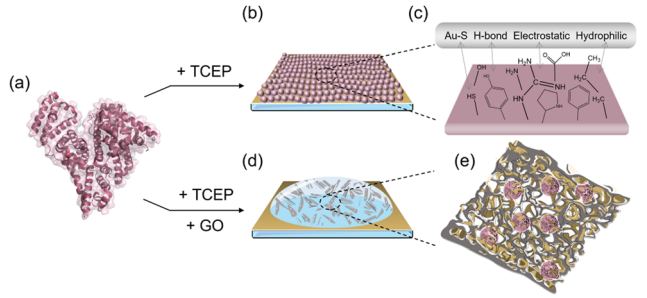

Fig. 1 Schematic for the preparation of dBSA and dBSA–GO nanofilms. (a)–(b) Assembling the dBSA nanofilm on an Au^{TS} surface with dBSA formed from TCEP-treated BSA. (c) Possible functional groups exposed on the dBSA nanofilm. (d) Construction of a dBSA–GO nanofilm on the Au^{TS} surface *via* drop-casting. (e) Structural configuration of the dBSA–GO nanofilm.

functional groups (Fig. 1a–c).[23,25] These characteristics give dBSA enhanced stability and greater potential as a humidity sensing material than native BSA. Graphene oxide (GO) is widely used in the field of humidity sensors due to its high surface-area-to-volume ratio, good porosity, and large amount of hydrophilic functional groups.[1,2,26] In this study, we enhanced both the proton conductivity and specific surface area by incorporating dBSA into GO (Fig. 1d and e). The fabricated humidity sensor possesses high robustness, exceptional selectivity, and rapid response. Remarkably, the current response ratio in the range of 15–90% RH reaches 7.0×10^6, which is more than four orders of magnitude higher than that of dBSA itself. With increasing RH, water enhances the current in two distinct ways, *i.e.*, permeation into the dBSA–GO nanofilm to improve proton conductivity, and adsorption onto its surface to alter dipole moments and increase current under forward bias. With these capabilities, applications such as respiratory and surrounding humidity monitoring have been successfully implemented, demonstrating the great prospects of the dBSA–GO nanofilm for humidity monitoring systems and contactless sensing devices.

2. Experimental section

2.1 Materials

Bovine serum albumin (BSA), 2-mercaptoethylamine·HCl (2-MEA), and eutectic gallium-indium (EGaIn) were purchased from Sigma-Aldrich. Tris(2-carboxyethyl) phosphine hydrochloride (TCEP), 5,5′-dithiobis (2-nitrobenzoic acid) (DTNB), thioflavin-T (ThT), and 8-anilino-1-naphthalenesulfonic acid (ANS) were purchased from Aladdin. NaOH, HF, acetone, and isopropyl alcohol were purchased from Sinopharm Chemical Reagent Co., Ltd. N_2, O_2, and Ar were purchased from Wuhan Zhongxin Ruiyuan Gas Co., Ltd. Au was purchased from China Pure New Materials (Beijing) Technology Co., Ltd. Graphene oxide (GO) prepared through a modified Hummers' method was purchased from Shenzhen Suiheng Graphene Technology Co., Ltd. Deionized water (18.2 MΩ cm) was purified using an ELGA PureLab Ultra Genetic Water Purification System.

2.2. Preparation of nanofilm

A BSA monolayer was prepared by immersing the templated-stripped Au (Au^{TS}) substrate in 2-MEA solution followed by BSA solution. dBSA nanofilms were assembled by incubating the Au^{TS} substrate in a mixed solution of TCEP and BSA followed by rinsing with water. GO nanofilm was fabricated by drop-casting GO solution onto Au^{TS} substrates. dBSA–GO hybrid nanofilm was prepared by mixing GO with dBSA solution and drop-casting the solution onto the Au^{TS} substrate. dBSA/GO nanofilm was created by alternately stacking dBSA nanofilm and GO nanofilm layer-by-layer on the Au^{TS} substrate. The details of sample preparations are provided in ESI,† Section S1.1.

2.3. Characterization

A J.A. Woollam M-2000 spectroscopic ellipsometer was used to measure the thickness of the BSA monolayer and dBSA nanofilms. The morphologies of the monolayer and nanofilms were obtained using atomic force microscopy (AFM, Park NX10). Kelvin probe measurements were also performed with the same instrument for work function analysis. Polarization modulation-infrared reflection–absorption spectra (PM-IRRAS) were obtained using a Bruker INVENIO R Fourier transform infrared spectrometer. Surface hydrophobicity was assessed with a POWEREACH® JC2000C contact angle measuring instrument. Secondary structures were analyzed *via* CD using a Jasco-810 spectropolarimeter. Fluorescence spectra were recorded using an RF-6000 fluorescence spectrophotometer (Shimadzu). UV-visible spectroscopy (Nanodrop One, Thermo Scientific) was utilized to quantify free thiol groups in dBSA solutions. More details are given in ESI,† Section S1.2.

2.4. Electrical measurements

The electrical measurements of Au^{TS}/nanofilms/GaO_x/EGaIn junctions were carried out in a humidity-controlled chamber. A Keithley 6430 Sub-Femtoamp Remote SourceMeter was used to obtain *J–V* curves with sweeps from 0 V → −0.5 V → +0.5 V → 0 V in steps of 10 mV and delays of 20 ms between steps. More than 7 junctions and 15 *J–V* traces per junction were measured on each sample. More than 400 *J* values at 0.5 V of the *J–V* traces from two or three parallel samples were collected for statistics. The *J–V* curves that conformed to the 95% confidence interval were collected and averaged for discussion.

To test the selectivity and response rate, *I–t* measurements were performed through the Au^{TS}/nanofilms/GaO_x/EGaIn junctions at 0.5 V, with a sampling interval of 0.1 s. Nitrogen, argon, and oxygen were supplied directly, while ethanol and water vapor were carried by a nitrogen flow. The flow rate and volume of the gases were controlled manually using valves. The current variation was observed as the gas flow alternated towards or away from the molecular junction. For the water vapor, the initial RH was 40%, while the water vapor carried by nitrogen was 75% RH. The current saturation and transient response rates were measured with the gas flow either constantly or intermittently near the molecular junction.

The impedance spectra of the Au^{TS}/nanofilms/GaO_x/EGaIn junctions were obtained with a potentiostat (Princeton Applied

Research VersaSTAT 3F). The data was recorded using VersaStudio software and fitted with an equivalent circuit in ZView® software. A frequency range of 1–5 × 10^4 Hz and a sinusoidal signal of 500 mV were used with 20 frequencies per decade and 5 repetitions per measurement.

3. Results and discussion

3.1. Preparation of dBSA–GO nanofilm

dBSA was obtained by mixing BSA with TCEP, which breaks the disulfide bonds of BSA and prevents it from re-oxidizing. The denaturization of BSA was confirmed through a series of characterizations in solution. Circular dichroism (CD) spectroscopy[27] showed changes from the negative peaks at 208 and 222 nm corresponding to the α-helix structure in native BSA to a negative peak at 216 nm corresponding to the β-sheet in dBSA, along with a dramatic decrease in peak intensity (Fig. 2a). Thioflavin T (ThT) can specifically stain amyloid-like assemblies rich in cross-β-sheet structures, producing enhanced fluorescence intensity.[28] Here, the fluorescence of ThT at 484 nm significantly increased after binding to dBSA instead of native BSA, identifying the conversion of the conformation and the formation of dBSA from native BSA (Fig. 2b). 8-Anilino-1-naphthalene sulfonic acid (ANS) can sensitively detect the exposure of hydrophobic groups on proteins, which

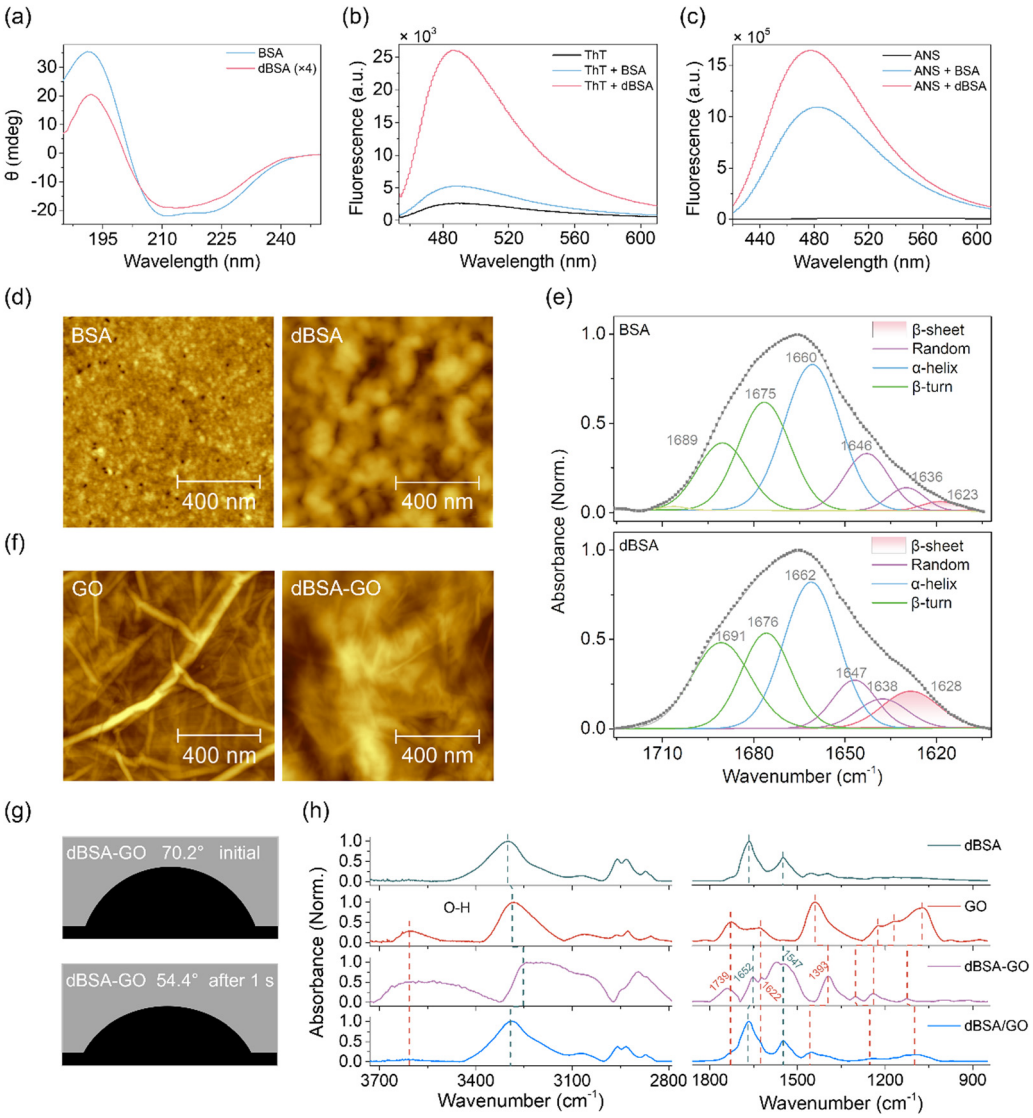

Fig. 2 Structural characterizations of dBSA in solution and BSA monolayer, dBSA, GO, dBSA/GO, and dBSA–GO nanofilms on Au^{TS} surfaces. (a) CD spectrum of dBSA in solution compared with that of native BSA. (b) ThT fluorescence and (c) ANS fluorescence in the presence of dBSA and native BSA (λ_{ex} = 440 nm for ThT and 398 nm for ANS, respectively). (d) Morphologies of the BSA monolayer and dBSA nanofilm (34 nm) on the Au^{TS} surface as observed *via* AFM. (e) PM-IRRAS of native BSA monolayer and dBSA nanofilm (34 nm) on the Au^{TS} surface. (f) Morphologies of the GO and dBSA–GO nanofilms on Au^{TS} surface as observed *via* AFM. (g) Water contact angles of the dBSA–GO nanofilm on the Au^{TS} surface at the initial state and after 1 second. (h) PM-IRRAS spectra of dBSA (34 nm), GO, dBSA–GO, and dBSA/GO nanofilms in the 3730–2790 cm^{-1} and 1860–840 cm^{-1} regions.

also manifests as enhanced fluorescence intensity.[29] Compared to the ANS–BSA mixture, the elevated fluorescence intensity of the ANS–dBSA mixture proved the increased exposure of hydrophobic groups (Fig. 2c). The Ellman reagent method using 5,5′-dithiobis(2-nitrobenzoic acid) also confirmed the presence of free thiol groups in dBSA (Fig. S1, ESI†).[30] All these results suggest that TCEP successfully broke the disulfide bonds of native BSA, leading to partial unfolding of the BSA structure. The exposure of hydrophobic groups due to the destruction of the α-helix structure of BSA leads to the aggregation of the unfolded protein and then the formation of a nanofilm at gas–liquid or solid–liquid interfaces.[31]

Here, the dBSA nanofilm was achieved by incubating freshly mixed BSA–TCEP solution on templated stripped Au (Au^{TS}) substrates. The degree of BSA denaturation in the dBSA nanofilms was adjusted through the incubation time. The dBSA nanofilms displayed uniform particle morphologies on Au^{TS} substrates characterized using AFM, with the dBSA size exceeding that of the native BSA self-assembled monolayer and increasing with incubation time (Fig. 2d and Fig. S2, ESI†). Correspondingly, the thicknesses of the dBSA nanofilms measured by ellipsometry also increases with incubation time (Table S1, ESI†). Additionally, the contact angle decreases with increscent dBSA size, indicating enhanced surface hydrophilicity (Fig. S3,ESI†). In the PM-IRRAS spectra, the amide I band of the dBSA nanofilm demonstrates a significant increase in the β-sheet content relative to that of the native BSA monolayer, which is consistent with the results of CD and ThT fluorescence in solution (Fig. 2e).[32,33] Moreover, longer incubation time leads to a greater transition from α-helical to β-sheet structure (Fig. S4, ESI†).

The dBSA solution was then mixed with GO solution and drop-casted on an Au^{TS} substrate to construct the dBSA–GO nanofilm. Here, a 34-nm dBSA nanofilm, drop-casted GO nanofilm, and a stacked nanofilm composed of dBSA (34 nm) and GO layers (dBSA/GO) were prepared for comparison. Both the dBSA/GO and dBSA–GO nanofilms exhibit the grained characteristics of dBSA and the crumpled morphologies of GO. The roughness averages (R_a) of the dBSA/GO, dBSA, GO, and dBSA–GO nanofilms are 22.7, 5.0, 3.6, and 84.7 nm, respectively. The film thicknesses of the GO, dBSA/GO, and dBSA–GO nanofilms are in the range of hundreds of nanometers (Fig. 2f and Fig. S5, ESI†). The water contact angles of the dBSA, GO, dBSA/GO, and dBSA–GO nanofilms are 67.3°, 61.5°, 80.2°, and 54.4°, respectively, indicating that the dBSA–GO nanofilm exhibits the best hydrophilicity among these four nanofilms (Fig. 2g and Fig. S3, and S6, ESI†). Moreover, in contrast to the unchanging contact angles of the other nanofilms over time, the water droplets on the dBSA–GO nanofilm collapsed rapidly within 1 second (Fig. 2g). This suggests that the blend of dBSA and GO may contribute to increased porosity specific surface area, thereby resulting in a remarkably high water absorption capacity.

To investigate the chemical structure of dBSA–GO and dBSA/GO nanofilms, the dBSA, GO, dBSA–GO, and dBSA/GO nanofilms were characterized using PM-IRRAS (Fig. 2h). Multiple peaks were observed for the dBSA–GO nanofilm. The peaks at 1652 cm^{-1} and 1547 cm^{-1} are the stretching vibration of the C═O bond and the bending vibration of the N–H bond in the amide group. The peak at 1622 cm^{-1} corresponds to the stretching vibration of the C═C bond. The peak at 1739 cm^{-1} is due to the C═O stretching vibration in carboxylic acid, while the peak at 1393 cm^{-1} is from the bending vibration of the O–H bond. The peaks within the range of 1000–1300 cm^{-1} are associated with the stretching vibration of the C–O bond. The above peaks would originate from the components of dBSA and GO, respectively. These peaks have significant shifts compared to those of the dBSA- and GO-only nanofilms, indicating the interactions between dBSA and GO in the dBSA–GO nanofilm. The dBSA/GO nanofilm also displayed similar infrared characteristic peaks, but with smaller shifts compared to the dBSA–GO nanofilm. The differences between the dBSA–GO and dBSA/GO nanofilms further supported the interactions of dBSA and GO in the dBSA–GO nanofilm. Additionally, in the 3000 cm^{-1} spectral region, the prominent redshift and broadening of the O–H peak in the dBSA–GO nanofilm suggested increasing hydrogen bonds. In summary, significant interactions between dBSA and GO occur in the dBSA–GO nanofilm, accompanied with increasing hydrogen bonding. These interactions fulfill the prerequisites for the formation of a widely connected hydrogen bonding network within the dBSA–GO nanofilm.

3.2. Humidity response test of dBSA–GO nanofilm

The humidity responses of the nanofilms under different RH conditions at room temperature were recorded using the current density (J) *via* the Au^{TS}/nanofilm/GaO_x/EGaIn junctions in a humidity-controlled chamber (Fig. S7, ESI†). A large number of J *versus* applied bias curves (J–V curves) were measured, and the statistical log$J$ values at +0.5 V under RH values from 15% to 90% were recorded for comparison (Fig. 3a and Fig. S8–S9, ESI†). The statistical data from more than 14 molecular junctions constructed from 2–3 samples was consistent, indicating the excellent reproducibility of the experimental results. The current response ratios, $\frac{J_{90\%RH}}{J_{15\%RH}}$, were further defined to evaluate the current response of the nanofilms to RH (Fig. 3b). In contrast to the lack of RH responsiveness of the BSA monolayer, the dBSA nanofilm (34 nm) exhibits a response ratio of 259. The J value at +0.5 V of the GO nanofilm is higher than that of the dBSA nanofilm and presents a positive RH response ratio of 433. Remarkably, the log$J$ value of the dBSA–GO nanofilm increases almost linearly from −7.74 to −0.90 as the RH increases from 15% to 90%. The current response ratio reaches 7.0×10^6 and is approximately four orders of magnitude larger than those of the GO and dBSA nanofilms. This current response ratio is even much greater than that of the dBSA/GO nanofilm, suggesting that the porous surface of the dBSA–GO nanofilm and hydrogen bonding between dBSA and GO may play an important role in the current response. The extent of the denaturation of dBSA is challenging to control when preparing dBSA–GO nanofilms. The J values at +0.5 V for dBSA nanofilms with varying degrees of denaturation were measured (Fig. S9, ESI†). The results show that the J values of the dBSA

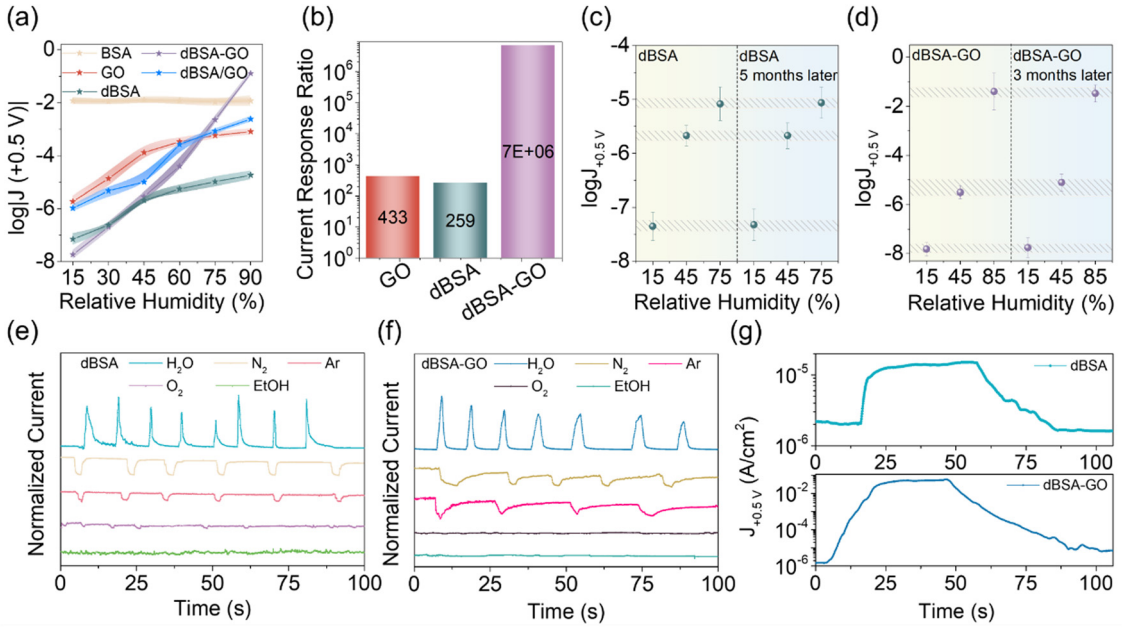

Fig. 3 Humidity responses of the nanofilms. (a) log J values of BSA monolayer, dBSA, GO, dBSA–GO, and dBSA/GO nanofilm junctions at +0.5 V under different RH levels. The error bars represent the 95% confidence interval range obtained from Gaussian fitting of at least 400 measurements. (b) Current response ratio of GO, dBSA, and dBSA–GO nanofilms between 15% and 90% RH. (c) and (d) Long-term stabilities of the dBSA nanofilm after 5 months (c) and dBSA–GO nanofilm after 3 months (d) under different RHs. The error bars show the 95% confidence interval obtained by performing Gaussian fitting on at least 200 measurements. (e) and (f) Normalized current changes of the dBSA (e) and dBSA–GO (f) nanofilms in various gases. The environmental ambient humidity (50% RH) serves as the testing background. The maximum response peaks of dBSA and dBSA–GO nanofilms in water vapor were each set to 1 for normalization of all the current changes in different gases. (g) Response rates for the dBSA and dBSA–GO nanofilms. The initial RH was 40% and increased with the H_2O flow. The 34 nm thick dBSA nanofilm was chosen for comparison.

nanofilms rise with increasing RH but drop with increasing particle size and film thickness, which is different from the behavior of BSA. The current response ratio is positive relative to the degree of BSA denaturation (Fig. S10, ESI†). Considering the cost, we also prepared the dBSA–GO nanofilm on an Ag^{TS} substrate using the same method as for the Au^{TS} substrate. The results in Fig. S11 (ESI†) showed that the current response ratio was consistent across both substrates, indicating that Ag is a viable low-cost alternative.

Having observed the excellent current response ratio of the dBSA–GO nanofilm, other aspects of its performance related to humidity sensing were evaluated and compared with the dBSA nanofilm. First, repeated testing of the same sample after 5 months for the dBSA nanofilm and 3 months for the dBSA–GO nanofilm showed stable log$J$ values with minimal variations (Fig. 3c and d). The maximum error was 7.3% for dBSA–GO nanofilm after 3 months at 45% RH, and 0.4% for the dBSA nanofilm after 5 months at 15% RH. Both the dBSA and dBSA–GO nanofilms exhibit good long-term stabilities and reliabilities for humidity response. Additionally, these results also reflect the ability of the sensor to recover effectively from exposure to high-RH environments, demonstrating good repeatability. Moreover, the current signals of the dBSA and dBSA–GO nanofilms respond differentially to gaseous substances, showing excellent selectivity in response to RH. The experiment included manual control of frequent airflows on the nanofilms with various strengths and rates. This led to possible differences in the magnitude and width among response signals. Despite the magnitude and width differences, H_2O induces increased current response, N_2 and Ar reduce the current, and ethanol vapor and O_2 have little effect on the current (Fig. 3e and f). The decreased current in response to N_2 and Ar should correlate with the reduced RH. In the nanofilm responses to RH changes, the J values take a few seconds to reach saturation in the presence of an H_2O flow and return to their initial level after removing the H_2O flow (Fig. 3g). Despite the several-second response and recovery times, the variation in the J values is large. The response rates of dBSA and dBSA–GO are increases of 0.12 and 0.18 orders of magnitude per second in the J values, respectively. This enables the detection of rapid changes in local humidity with high sensitivity. For instance, when a brief pulse of H_2O flow ($\sim$1 s) was applied, the nanofilms rapidly generated prominent J value changes that significantly higher than the signal-to-noise ratio. Moreover, the J value for the dBSA nanofilm increased 8.4-fold relative to the initial J value, whereas the J value for the dBSA–GO nanofilm was enhanced 49.8-fold (Fig. S12, ESI†). Overall, the stability and selectivity of the dBSA–GO nanofilm are comparable to those reported for GO in the literature[2] and the dBSA nanofilm, but its response rate is superior to both. Moreover, as shown in Table S2 (ESI†), the dBSA–GO nanofilm shows significant advantages in terms of response ratio and stability compared to other GO- or BSA-based humidity sensors.

The ultra-thin and crumpled structure of GO exhibits a large specific surface area and is capable of efficiently adsorbing and desorbing water.[26,34] Additionally, the increase in β-sheet

content and exposure of a significant number of hydrophilic groups enhance proton conduction in the dBSA nanofilm, thereby facilitating a more sensitive response to the subtle changes in humidity. After the combination of dBSA and GO, the rapid decrease in contact angle within 1 second and the rougher surface indicate the significant larger specific surface area of the dBSA–GO nanofilm compared to that of the GO nanofilm. Moreover, the increasing hydrogen bonding interactions between dBSA and GO further enhance the humidity-related proton conductivity, surpassing that of the dBSA-only nanofilm. Consequently, we have achieved superior current responsiveness to water molecules in the composite dBSA–GO nanofilm compared to that of the dBSA- or GO-only nanofilms. Additionally, both the protein and the GO are biocompatible, ensuring the safety and sustainability of the sensor in environmental and biological applications.

3.3. Mechanism of water molecule interaction with the dBSA–GO nanofilm

Water molecules induce current changes through two main binding modes. First, intermolecular hydrogen bonds among water molecules, dBSA, and GO promote proton conduction within the nanofilm. Second, the adsorption of water molecules onto the surface alters the net dipole moment, causing asymmetric current response. To ascertain the roles of water in forming hydrogen bonds within the nanofilm, we conducted *I–t* testing at different RH values (Fig. S13, ESI†). The transient currents at different RH levels all exhibited time-dependent decays before reaching a steady state, indicating a brief initial capacitive response. This phenomenon is associated with the accumulation of charge at the proton-blocked Au^{TS} electrode, indicating the occurrence of proton transport.[35] To better elucidate the capacitive and resistive contributions to the response of the nanofilms, we conducted impedance spectroscopy experiments. The Nyquist plots of the dBSA and dBSA–GO nanofilms display capacitive arc trends, which could be fitted using an equivalent circuit with a resistor and a constant phase element (CPE) in parallel (Fig. 4a and Fig. S14, ESI†). The residual within 10% in the Kramers–Kronig transforms and the single peak in each distribution of relaxation time illustrate the validity of the IS data and the rationality of the equivalent circuit, respectively (Fig. S15 and S16, ESI†). The resistance and capacitance of the dBSA and dBSA–GO nanofilm junctions were obtained from fitting of the IS results (Fig. 4b). As the RH increased from 15% to 45%, the resistance decreased by more than 94% and 95% of the total reduction $\left(\frac{R_{15\%} - R_{45\%}}{R_{15\%} - R_{90\%}}\right)$ for the dBSA and dBSA–GO nanofilms, respectively, while the capacitance remained relatively unchanged. Conversely, when the RH increased from 45% to 90%, the capacitance increased over 94% and 100% of the total increment $\left(\frac{C_{90\%} - C_{45\%}}{C_{90\%} - C_{15\%}}\right)$ for the dBSA and dBSA–GO nanofilms, respectively, while the resistance showed almost no change. The falling resistance and rising capacitance at high RH indicate the dominance of

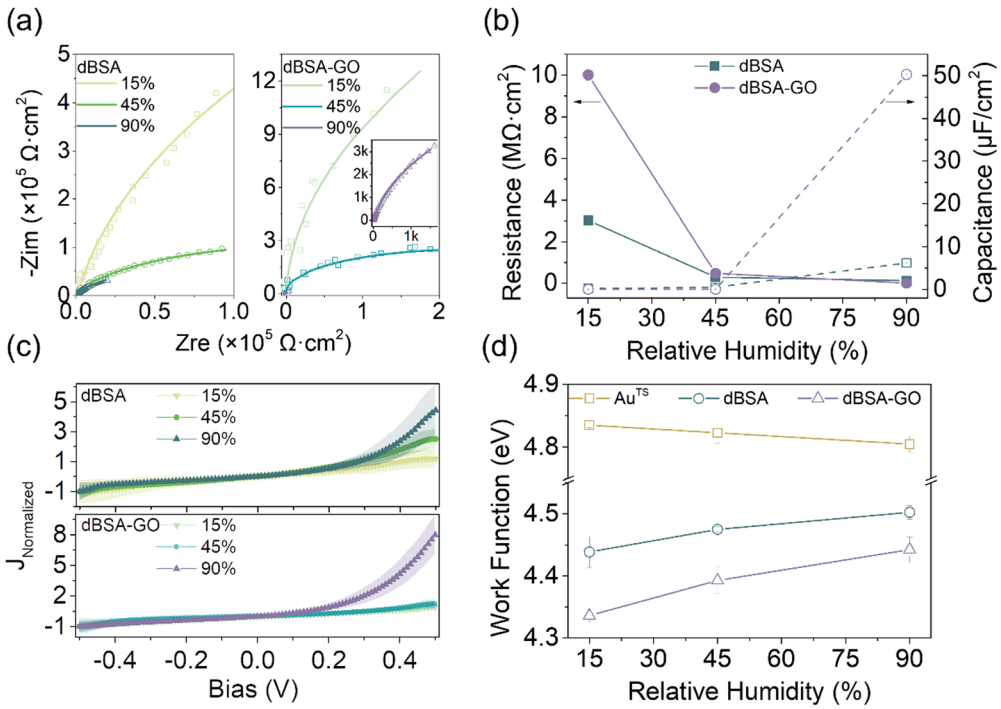

Fig. 4 Proton transport in the humidity responsive process in the sensors. (a) Impedance spectra of the dBSA and dBSA–GO nanofilm junctions at different RH values. (b) Resistance (solid lines) and the capacitance (dashed lines) of the dBSA and dBSA–GO nanofilm junctions *vs.* RH. (c) Normalized *J* values of dBSA and dBSA–GO nanofilm junctions *vs.* bias at various RH values. The 95% confidence interval ranges shown by the error bars were determined through Gaussian fitting of no fewer than 450 measurements. (d) Work function of dBSA and dBSA–GO nanofilms on Au^{TS} at different RH values compared with that of bare Au^{TS}. The error bars were derived from three repeated experiments.

proton transport and the accumulation of protons at electrode interfaces in the nanofilm junctions at high RH, which is closely related to the water absorption. Correspondingly, a high current response to humidity is achieved.

Additionally, the adsorption of water on the surface further induced the asymmetry of the *J–V* curves.[36,37] The normalized *J–V* curves demonstrate that the current ratios $\left(\frac{J_{+0.5V}}{J_{-0.5V}}\right)$ of the dBSA and dBSA–GO nanofilms increase with RH. The current ratio of the dBSA–GO nanofilm grows more than that of the dBSA nanofilm (Fig. 4c). In contrast, the BSA monolayer exhibits symmetric *J–V* curves under these RH values (Fig. S17, ESI†). The relative increases in the *J* values at a positive bias with RH are likely caused by the dipole of the water molecules gradually adsorbing on dBSA and dBSA–GO nanofilms and the induced local electric fields superimposed on the applied field, although the direction of the dipole require further discussion.[36–38] The work functions of the Au^{TS} electrodes with attached nanofilms were determined through Kelvin probe force microscopy measurements (Fig. 4d). The work function of the Au^{TS} substrate exhibited a negligible change (within 30 meV) in the RH range from 15% to 90%. In contrast, the work functions of the dBSA and dBSA–GO nanofilms modified Au^{TS} changed monotonically by 64 meV and 106 meV over the same RH range, respectively, which is consistent with the unidirectional current increases with RH at a positive bias. This indicates that the water dipole does play roles in the energy band of the Au^{TS} electrode. The gradual adsorption of the polar water monotonically shifts the net dipole moment of the dBSA and dBSA–GO nanofilms and thus alters the energy barrier of the nanofilm junction, which in turn directly tunes the degree of asymmetry of the *J–V* curves and promotes the sensitivity with higher *J* values at a positive bias. Based on the *I–t* testing, impedance, and Kelvin probe results for both the dBSA and dBSA–GO nanofilms, the roles of water are similar in these nanofilms. However, in the dBSA–GO nanofilm, the changes in the transient current decay, capacitance, and work function with increasing humidity are greater than those of the dBSA nanofilm, indicating stronger interaction of water with the dBSA–GO nanofilm, both in the interior and on the surface.

3.4. Application of dBSA–GO humidity sensor

Given the rapid response and high sensitivity of the dBSA–GO sensor, it was used to monitor human breathing (Fig. 5 and Fig. S18, ESI†). Exhaled air from the mouth or nose contains water, which alters the surrounding humidity and thereby changes the current flowing through the sensor. The dBSA–GO sensor successfully detected and recorded the periodic current response to changes in breathing (Fig. 5a). Compared to that from the nose, gas exhaled from the mouth contained a higher concentration of water molecules, leading to a more pronounced variation in the current signal. Fig. 5b shows the current response of the sensor to the rate of nose breathing. Normal, fast, and slow breathing can be clearly distinguished

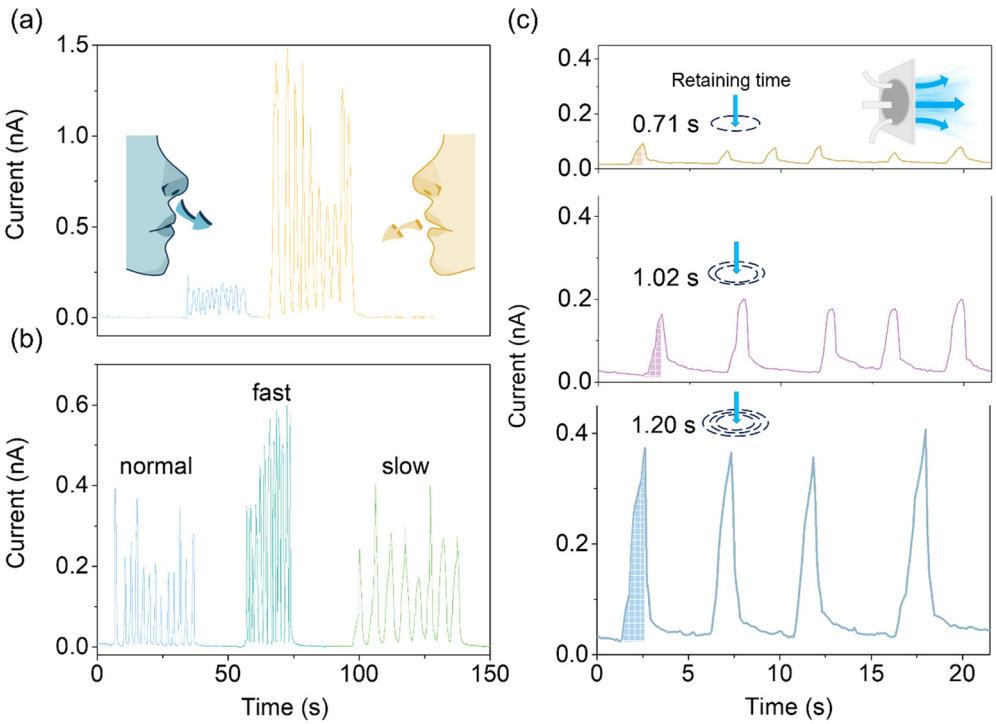

Fig. 5 Applications of the dBSA–GO humidity sensor. (a) Respiratory response curves for nose and mouth breathing. (b) Response curve for nose breathing at different breathing rates. The distance of the sensor to nose or mouth was approximately 10 cm, but this is not the testing distance limitation of the sensor to detect humidity. (c) Dynamic current response in the presence of wet filter paper placed alternately close to and far from the sensor. From top to bottom, the time for which the filter paper was kept close to the sensor increases.

based on the frequency of the current response, as fast breathing means that water molecules more quickly accumulate near the sensor, resulting in a relatively greater change in current than normal and slow breathing. To explore the potential application of humidity sensors in non-contact switches, a wet filter paper with nitrogen flowing through it was used as a humidity source to simulate the humidity distribution. The filter paper was alternately placed close to and far from the sensor, with the closest distance being about 1 cm. A larger current response was observed as the filter paper remained close to the sensor for a longer time (Fig. 5c). This was similar to long- or short-time presses triggering different current responses from the sensor.

4. Conclusion

An ultrasensitive dBSA–GO humidity sensor has been developed for human respiratory monitoring and non-contact sensing by doping dBSA with GO. dBSA possesses a higher proportion of β-sheet structures due to the denaturation process, which facilitates proton transfer. GO has a large specific surface area and abundant water adsorption functional groups. The combination of dBSA and GO results in a greater specific surface area with a porous surface and enhanced proton conductivity capacity, leading to an augmented current signal response to RH. During the humidity elevation process, the adsorbed water molecules on the dBSA–GO nanofilm not only form hydrogen bonds with dBSA and GO, but also alter the dipole moment of the nanofilms and the work function of the electrodes. These facilitate efficient proton conduction and enhance the current at a positive bias, both of which contribute to an unprecedented current response ratio of nearly 7 orders of magnitude between RH values of 15–90% with excellent stability, selectivity, and response rate. The dBSA–GO sensor was successfully applied to monitor human breathing under various situations and simulate human–computer interaction scenarios. This work demonstrates that structural deformation and doping of proton-conductive proteins is an effective strategy for the design of humidity sensors.

Data availability

The authors confirm that the data supporting the findings of this study are available within the article and its ESI.†

Conflicts of interest

There are no conflicts to declare.

Acknowledgements

This work was supported by the financial support from the National Natural Science Foundation of China (22374109 and 21974102) and the National Key R&D Program of China (2018YFA0703700).

References

1 L. Lu, C. Jiang, G. Hu, J. Liu and B. Yang, *Adv. Mater.*, 2021, **33**, 2100218.
2 D. Lei, Q. Zhang, N. Liu, T. Su, L. Wang, Z. Ren, Z. Zhang, J. Su and Y. Gao, *Adv. Funct. Mater.*, 2022, **32**, 2107330.
3 S. M. S. Rana, M. A. Zahed, M. T. Rahman, M. Salauddin, S. H. Lee, C. Park, P. Maharjan, T. Bhatta, K. Shrestha and J. Y. Park, *Adv. Funct. Mater.*, 2021, **31**, 2105110.
4 N. Li, Y. Jiang, C. Zhou, Y. Xiao, B. Meng, Z. Wang, D. Huang, C. Xing and Z. Peng, *ACS Appl. Mater. Interfaces*, 2019, **11**, 38116–38125.
5 H. Yan, S. Guo, F. Wu, P. Yu, H. Liu, Y. Li and L. Mao, *Angew. Chem., Int. Ed.*, 2018, **57**, 3922–3926.
6 Y. Li, M. Zhang, X. Hu, L. Yu, X. Fan, C. Huang and Y. Li, *Nano Today*, 2021, **39**, 101214.
7 T. Wu, S. Gao, W. Wang, J. Huang and Y. Yan, *ACS Appl. Mater. Interfaces*, 2021, **13**, 41997–42004.
8 Q. Hua, J. Sun, H. Liu, R. Bao, R. Yu, J. Zhai, C. Pan and Z. L. Wang, *Nat. Commun.*, 2018, **9**, 244.
9 X. Chen, Y. Li, X. Wang and H. Yu, *ACS Appl. Mater. Interfaces*, 2022, **14**, 36227–36237.
10 E. Torres Alonso, D. W. Shin, G. Rajan, A. I. S. Neves, S. Russo and M. F. Craciun, *Adv. Sci.*, 2019, **6**, 1802318.
11 D. Zhang, X. Zong, Z. Wu and Y. Zhang, *ACS Appl. Mater. Interfaces*, 2018, **10**, 32631–32639.
12 X. Liu, T. Fu, J. E. Ward, H. Gao, B. Yin, T. Woodard, D. R. Lovley and J. Yao, *Adv. Electron. Mater.*, 2020, **6**, 2000721.
13 J. Yang, R. Shi, Z. Lou, R. Chai, K. Jiang and G. Shen, *Small*, 2019, **15**, 1902801.
14 J. Yu, Y. Feng, D. Sun, W. Ren, C. Shao and R. Sun, *ACS Appl. Mater. Interfaces*, 2022, **14**, 10886–10897.
15 S. Mondal, Y. Agam, R. Nandi and N. Amdursky, *Chem. Sci.*, 2020, **11**, 3547–3556.
16 Y. Agam, R. Nandi, T. Bulava and N. Amdursky, *Mater. Adv.*, 2021, **2**, 1739–1746.
17 N. Amdursky, E. D. Głowacki and P. Meredith, *Adv. Mater.*, 2018, **31**, 1802221.
18 R. Rimeika, D. Čiplys, V. Poderys, R. Rotomskis and M. S. Shur, *Sens. Actuators, B*, 2017, **239**, 352–357.
19 M. Sasmal, S. Majumder and T. K. Bhattacharyya, *IEEE Sens. J.*, 2018, **18**, 8223–8229.
20 S. Bhattacharya and M. Sasmal, *IEEE Trans. NanoBiosci.*, 2016, **15**, 27–33.
21 M. Sasmal, T. K. Maiti and T. K. Bhattacharyya, *IEEE Sens. J.*, 2016, **16**, 1510–1517.
22 R. Nandi, Y. Agam and N. Amdursky, *Adv. Mater.*, 2021, **33**, 2101208.
23 X. Hu, J. Tian, C. Li, H. Su, R. Qin, Y. Wang, X. Cao and P. Yang, *Adv. Mater.*, 2020, **32**, 2000128.
24 Y. Liu, S. Miao, H. Ren, L. Tian, J. Zhao and P. Yang, *Nat. Protoc.*, 2024, **19**, 539–564.
25 S. Bolisetty and R. Mezzenga, *Nat. Nanotechnol.*, 2016, **11**, 365–371.
26 S. Borini, R. White, D. Wei, M. Astley, S. Haque, E. Spigone, N. Harris, J. Kivioja and T. RyhäNen, *ACS Nano*, 2013, **7**, 11166–11173.

27 A. Micsonai, F. Wien, L. Kernya, Y.-H. Lee, Y. Goto, M. Réfrégiers and J. Kardos, *Proc. Natl. Acad. Sci. U. S. A.*, 2015, **112**, 3095–3103.
28 R. Khurana, C. Coleman, C. Ionescu-Zanetti, S. A. Carter, V. Krishna, R. K. Grover, R. Roy and S. Singh, *J. Struct. Biol.*, 2005, **151**, 229–238.
29 D. I. Cattoni, S. B. Kaufman and F. L. Gonzalez Flecha, *Biochim. Biophys. Acta*, 2009, **1794**, 1700–1708.
30 J. R. Winther and C. Thorpe, *Biochim. Biophys. Acta, Gen. Subj.*, 2014, **1840**, 838–846.
31 Y. Liu, F. Tao, S. Miao and P. Yang, *Acc. Chem. Res.*, 2021, **54**, 3016–3027.
32 P. Wang and J. Laskin, *Angew. Chem., Int. Ed.*, 2008, **47**, 6678–6680.
33 M. Goel, E. N. Marsh, Z. Chen and N. L. Abbott, *Langmuir*, 2014, **30**, 7143–7151.
34 A. J. Carr, S. E. Lee and A. Uysal, *Nanoscale*, 2023, **15**, 14319–14337.
35 N. Turetta, M. A. Stoeckel, R. Furlan De Oliveira, F. Devaux, A. Greco, C. Cendra, S. Gullace, M. Gicevicius, B. Chattopadhyay, J. Liu, G. Schweicher, H. Sirringhaus, A. Salleo, M. Bonn, E. H. G. Backus, Y. H. Geerts and P. Samori, *J. Am. Chem. Soc.*, 2022, **144** 2546–2555.
36 Y. Ai, A. Kovalchuk, X. Qiu, Y. Zhang, S. Kumar, X. Wang, M. Kuhnel, K. Norgaard and R. C. Chiechi, *Nano Lett.*, 2018, **18**, 7552–7559.
37 L. Tian, X. Song, X. Yu and W. Hu, *J. Phys. Chem. C*, 2021, **125**, 21614–21623.
38 H. Atesci, V. Kaliginedi, J. A. Celis Gil, H. Ozawa, J. M. Thijssen, P. Broekmann, M.-A. Haga and S. J. Van Der Molen, *Nat. Nanotechnol.*, 2018, **13**, 117–121.